applied sciences

MDPI

Article

Solar Ultraviolet Irradiance Characterization under All Sky Conditions in Burgos, Spain

Sol García-Rodríguez [1], Ignacio García [1,2], Ana García-Rodríguez [1], Montserrat Díez-Mediavilla [1] and Cristina Alonso-Tristán [1,*]

[1] Research Group Solar and Wind Feasibility Technologies (SWIFT), Electromechanical Engineering Department, Universidad de Burgos, 09006 Burgos, Spain
[2] Institute of Smart Cities (ISC), Department of Engineering, Public University of Navarre, Campus Arrosadía, 31006 Pamplona, Spain
* Correspondence: catristan@ubu.es or cristinaalonso.tristan@gmail.com; Tel.: +34-947-258853

Featured Application: The ratio between global horizontal ultraviolet irradiance and broadband solar horizontal irradiance is presented, and its dependency on sky cloudiness conditions, as defined by the CIE Standard sky classification and clearness index, is shown in this paper. A single pattern that is only dependent on sky conditions is discerned, regardless of the temporal basis of the study.

Abstract: Solar Ultraviolet Radiation (UVR), which is identified as a major environmental health hazard, is responsible for a variety of photochemical reactions with direct effects on urban and aquatic ecosystems, human health, plant growth, and the deterioration of industrial systems. Ground measurements of total solar UVR are scarce, with low spatial and temporal coverage around the world, which is mainly due to measurement equipment maintenance costs and the complexities of equipment calibration routines; however, models designed to estimate ultraviolet rays from global radiation measurements are frequently used alternatives. In an experimental campaign in Burgos, Spain, between September 2020 and June 2022, average values of the ratio between horizontal global ultraviolet irradiance (*GHUV*) and global horizontal irradiance (*GHI*) were determined, based on measurements at ten-minute intervals. Sky cloudiness was the most influential factor in the ratio, more so than any daily, monthly, or seasonal pattern. Both the CIE standard sky classification and the clearness index were used to characterize the cloudiness conditions of homogeneous skies. Overcast sky types presented the highest values of the ratio, whereas the clear sky categories presented the lowest and most dispersed values, regardless of the criteria used for sky classification. The main conclusion, for practical purposes, was that the ratio between *GHUV* and *GHI* can be used to model *GHUV*.

Keywords: UV; global irradiance; sky conditions; CIE standard sky classification; k_t; statistical analysis

Citation: García-Rodríguez, S.; García, I.; García-Rodríguez, A.; Díez-Mediavilla, M.; Alonso-Tristán, C. Solar Ultraviolet Irradiance Characterization under All Sky Conditions in Burgos, Spain. *Appl. Sci.* **2022**, *12*, 10407. https://doi.org/10.3390/app122010407

Academic Editors: Harry D. Kambezidis and Basil Psiloglou

Received: 19 September 2022
Accepted: 11 October 2022
Published: 15 October 2022

1. Introduction

Although Solar Ultraviolet Radiation (UVR) comprises only 8.73% of the solar radiation spectrum [1], its study is of great interest, due to its direct consequences for life on Earth. UVR is a major environmental hazard that causes health problems such as sunburn, skin cancer, photokeratitis, and ocular diseases, among others [2]; however, the natural synthesis of Vitamin D requires exposure to UVR [3]. UVR is also responsible for a variety of photochemical reactions, with direct effects on urban ecosystems [4]; for instance, the degradation of photovoltaic systems [5], stunted plant growth and morphology [6], and the equilibrium of aquatic ecosystems [7]. The spread and seasonality of several diseases have been linked to solar UVR [8–10]. UVR ground measurements are key to the analysis of its spatial and temporal distributions under different atmospheric conditions, and for public information campaigns on protection against UVR damage [11].

UVR is divided into three wavebands: UV-C (100–280 nm), UV-B (280–315 nm), and UV-A (315–400 nm). UV-C is absorbed in the stratosphere, whereas both the UV-A and the UV-B bands reach ground level in amounts that depend on several factors. Column ozone content, atmospheric composition [12] (aerosols, water vapor, and other gases), cloud type and distribution [13,14], and geometrical and geographic variables, such as solar zenith angle, and surface albedo [15,16], all contribute to UVR variability; however, it is difficult to evaluate the individual role of each variable, due to their combined effects with other variables under different atmospheric conditions [17].

UVR ground measurements are scarce, and spatial and temporal coverage around the globe is limited, which is mainly due to equipment maintenance costs and the complexities of measurement equipment calibration routines [17–19]; however, the models used to estimate solar UVR from global radiation measurements, with relatively few data inputs, are frequently used alternatives [11,12,15,20–36].

Several authors have studied the influence of clouds and sky conditions on surface UV measurements [12,13,17,22,33,37,38]. The presence of cloud cover and its type and distribution can both enhance total solar UVR by as much as 15% and reduce it by over 50%; this is due to the superposition of the albedo reflection, and distribution and extinction effects [39]. Conversely, atmospheric pollution and dust can drastically reduce total solar UV irradiance [33,40,41].

The ratio of global horizontal ultraviolet irradiance (*GHUV*) and global horizontal irradiance *(GHI)*, measured using different (ten-minute data intervals, hourly and daily values, and monthly and annual averages) time scales around the world and under different sky conditions, has been widely studied, as shown in the literature review summarized in Table 1. As is evident, the *GHUV*:*GHI* ratio ranges between 2.9 and 7%, with the highest values of the ratio corresponding to cloudy days, regardless of the index used for sky condition classification. The scattering effects on the UVR band caused by cloud cover increases the intensity of the *GHUV*, whereas the stronger absorption effect of water vapor on the infrared band contributes to lower levels of *GHI* [33]. The location of the measurement site is another important factor: *GHUV* at ground level increases when the site is closer to the Equator [42] and at a higher height above sea level (h.a.s.l.), due to the shorter optical length of rays through the atmosphere [43–45]. On a summer's day, *GHUV* is strongest at around noon when 50–60% of solar UVR can be measured. The solar zenith angle also affects the intensity of UVR: *GHUV* increases with the solar zenith angle, because solar UV rays, perceived as solid angles, are distributed over larger surface areas of the globe [16].

Table 1. Experimental measurements of the *GHUV*:*GHI* ratio around the world.

Ref.	Experimental Campaign	Location	Geographical Data	Height above Sea Level	*GHUV*/*GHI*	Comments
[46]	Austral summers 1978–1981	Amundsen-Scott South Pole Station	lat. 90° S	2835 m	4–4.3% (hourly av.)	Sun elevation > 17° Clear skies
[47]	30 min 1985–1987	Safat (Kuwait)	lat. 29°20′ N long. 47°57′ E	0 m	4.2–5.2% (monthly av.)	No sky classification
[48]	60 min 1985–1987	Dhahran (Saudi Arabia)	lat. 26°32′ N long. 50°13′ E	17 m	3.3–3.7% (monthly av.)	Sky conditions classified by k_t
[49]	60 min 01/01/1987–31/05/1988	Makkah (Saudi Arabia)	lat. 21.5° N long. 39.8° E	277 m	2.8–4.3% (monthly av.)	Sky conditions classified by k_t
[50]	2 min 01/04/1985–31/04/1988	Potsdam 1 (Germany)	lat. 52°22′ N long. 13°5′ E	35 m	3–4% (2 min av.)	No sky classification
[51]	10 min 03/1991–09/1991	Valencia (Spain)	lat. 39°28′00″ Nlong. 0°22′30″ W	40 m	2.7–3.2% (monthly av.)	Sky conditions classified by k_t

Table 1. *Cont.*

Ref.	Experimental Campaign	Location	Geographical Data	Height above Sea Level	*GHUV*/*GHI*	Comments
[52]	1990–1992	Cairo (Egypt)	lat. 30°05′ N long. 31°17′ E	23 m	2.7–3.4% (monthly av.)	All sky conditions
		Aswan (Egypt)	lat. 23°58′ N long. 32°47′ E	106 m	3.5–3.9% (monthly av.)	
[12,25,53]	1 min 1994–1995	Granada (Spain)	lat. 37.18° N long. 3.58° W	600 m	3–5% (monthly and hourly av.)	Sky conditions classified by k_t
					3.7–4% (1 min and 5 min av.) 4% (hourly av.) 3.4–4.6% (hourly av.)	Sky conditions classified by cloud cover (octas) All sky types
[53]	5 min 1993–1995	Almería (Spain)	lat. 36.83° N long. 2.41° W	0 m	3.7% (hourly av.)	All sky types
[30,54]	10 min 1991–1996 5 min 1996–1998	Valencia (Spain)	lat. 39°30′ N long. 0°25′ W	40 m	3.2% (10 min av.) 2.9–2.5% (hourly av.) 2.9–3.4% (daily av.)	Sky conditions classified by k_t
					4.4–5.6% (monthly av.)	
[23]	5 min 1996–1998	Cordoba (Spain)	lat. 37° 51′ N long. 4°48′ W	125 m	3.9–4.5% (monthly av.)	
[55]	60 min 03/1996–12/2000	Athens (Greece)	lat. 37.97° N long. 23.67° E	20 m	4.06% (monthly av.)	
[15]	1 min 06/1998–08/2001	Kwangju (South Korea)	lat. 35°10′ N long. 126°53′ E	90 m	7–9.4% (monthly av.)	Sky conditions classified by k_t
[56]	10 min 2004	Athalassa (Cyprus)	lat. 35°15′ N long. 33°40′ E	165 m	2.92–3.95% (hourly av.) 2.85–3.68% (daily av.)	Sky conditions classified by k_t
[57]	1 min 2005–2006	Lhasa (China)	lat. 29°30′ N long. 91°6′ E	3668 m	3.9–5% (monthly and daily av.)	Sky conditions classified by k_t
		Haibei (China)	lat. 37°37′ N long.101°19′ E	3230 m	3.7–4.6% (monthly and daily av.)	
[24,58,59]	5 min 2001–2005	Botucatu (Brazil)	lat. 22°530 S long.48°260′ W	786 m	4–4.9% (hourly av.) 4–4.8% (daily av.)	Sky conditions classified by k_t (four intervals)
[11]	5 min 2008	Maceió (Brazil)	lat. 9°280′ S long. 35°490′ W	127 m	2.3–3.6% (daily av.)	Sky conditions classified by k_t
[22]	10 min 02/2001–06/2008	Valladolid (Spain)	lat.41°40′ N long. 4°50′ W	840 m	3.8–4.4% (monthly and hourly av.) 3.8–4.2% (monthly and daily av.)	Sky conditions classified by cloud cover
[13,60]	1 min 2006–2012	Wuhan (China)	lat. 30°32′ N long. 114°21′ E	30 m	3.9–4.4% (daily av.) 3.8–4.3% (hourly av.) 3.96–4.94% (monthly av.)	Sky conditions classified by k_t
[18]	2005–2012	Sanya (China)	lat. 18°13′ N long. 109°28′ E	1.5 m	4.2–4.7% (monthly and hourly av.) 4.1–4.6% (monthly and daily av.)	Sky conditions classified by k_t

This study focuses on the determination of the *GHUV*/*GHI* ratio in Burgos (Spain), and its dependency on sky conditions, which is classified using different criteria. Experimental data of *GHUV*, *GHI*, and the sky luminance distribution were compiled from experimental sky scanner measurements. A complete statistical analysis of the results over different time scales (10 min, hourly, daily, monthly, and seasonal intervals) was completed. The results collected under different sky conditions, classified in accordance with the CIE standard sky taxonomy [61] and clearness index (k_t), were tested during a 22 month experimental test campaign.

The experimental facility, the measurement campaign, and the quality filters applied to the experimental data are described in Section 2. In Section 3, the description of the sky conditions in Burgos during the experimental campaign is presented, as well as a complete analysis of the quality of the experimental data and an analysis of the *GHUV*/*GHI* ratio over different temporal intervals and against sky classification criteria. Finally, the main results and the conclusions of the study are summarized in Section 4.

2. Experimental Data

All meteorological and radiometric experimental data used in this study were recorded at the weather station of the SWIFT Research Group, located on the roof of the Higher Polytechnic School building (EPS) of Burgos University (42°21′04″ N, 3°41′20″ W, 856 m above mean sea level). Figure 1 shows the location of the meteorological station on the flat roof of the EPS building, which is where the climatic parameters were measured. These parameters were as follows: ambient temperature, relative humidity, atmospheric pressure, wind speed and direction, and rainfall. A Kipp & Zonen CUV5 sensor was used to measure *GHUV*. *GHI* data were measured with a (Hulseflux, model SR11) pyranometer. Sky luminance and radiance distributions were determined with a commercial MS-321LR sky scanner manufactured by EKO Instruments (EKO Instruments Europe B.V. Den Haag, The Netherlands). The technical specifications of the various measurement instruments are shown in Tables 2–4. A complete description of the experimental facility and its location can be found in previous papers [62,63].

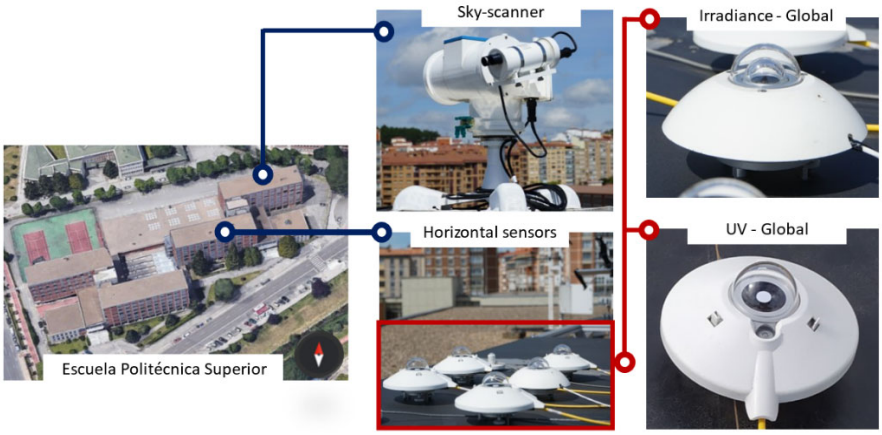

Figure 1. Location of the experimental equipment on the roof of the Higher Polytechnic School building at the University of Burgos (Spain).

Table 2. UV Radiometer technical specifications.

Model	CUV5
Spectral Range (Nominal passband 50% point)	300–385 nm
Spectral range (Overall)	280 to 400 nm
Sensitivity	300–500 $\mu V/(W/m^2)$
Temperature response (−40 °C–80 °C)	<−0.3%/°C
Directional response (up to 70° with 100 W/m^2 UV beam)	$< 5\ W/m^2$

Table 3. Pyranometer technical specifications.

Model	SR11
ISO classification	first class
Spectral range	285 to 3000 nm
Irradiance range	0 to 2000 W/m^2
Sensitivity	15 $\mu V/(W/m^2)$
Temperature response (−10 °C–40 °C)	±2%
Directional error	±20 W/m^2
Calibration uncertainty	<1.8%
Non-Stability	<±1% change per year
Tilt Error (0 to 90° at 1000 W m^{-2})	<±2%
Level Accuracy	<1%

Table 4. Sky scanner technical specifications.

Model	MS-321LR Sky Scanner
FOV	11°
Luminance	0 to 50 kcd/m^2
Radiance	0 to 300 W/m^2
A/D Convertor	16 bits
Calibration Error	2%

The experimental campaign ran from 14 September 2020 to 6 June 2022. *GHI* and *GHUV* data were recorded every 10 min (average recorded scans of 30 s). Experimental *GHI* data were subjected to the Quality Control (QC) procedure proposed for the MESoR project [64]. Regarding UV data, it was established that *GHUV* could not be higher than the extraterrestrial UV on the horizontal plane (UVH_0) that corresponded with the same time frame. UVH_0 was calculated with the correction factor (f_c) applied to the UV solar constant (UV_{sc}); this is based on the estimated orbital eccentricity multiplied by the cosine of the solar zenith angle, as shown in Equation (1).

$$UVH_0 = f_c UV_{sc} \cos\theta_z. \quad (1)$$

In the absence of a standardized value, the UV_{sc} was obtained from the integration of the solar spectrum, as revised by Gueymard [65], between 280 and 400 nm, subsequently obtaining a value of 102.15 W·m^{-2}. Data corresponding to solar elevation angles lower than 5° were discarded, in order to avoid the cosine response problems of the *GHI* and *GHUV* measurement instruments.

The sky scanner was adjusted monthly so that it could take measurements from sunrise to sunset. It completed a full scan in four minutes and started a new scan every ten minutes. Data that were not within the specifications (i.e., $\alpha_s \leq 7.5°, > 50$ kcd·m^{-2} and < 0.1 kcd·m^{-2}) were discarded. If a dataset (*GHI*, *GHUV*, or sky scanner measurement) failed to pass the QC, then all the simultaneous datasets were rejected; thus, 24.9% of the data recorded during the 22 month experimental campaign were rejected after failing the quality control tests, resulting in 34,270 valid 10 min data points. The seasonal data distribution was 22.8% in winter, 30.5% in spring, 20.3% in summer, and 26.3% in autumn.

Table 5 shows the annual and seasonal mean values of *GHI*, *GHUV*, temperature (*T*), relative humidity (*RH*), and wind speed (*WS*), which were calculated from the 10 min records. These values were obtained for the whole year and they were classified according to each sky type, k_t (overcast $0 \leq k_t \leq 0.35$, partly cloudy $0.35 < k_t \leq 0.65$, clear sky $0.65 < k_t \leq 1$) [66].

Table 5. Seasonal 10 min mean values (N) between 14 September 2020 and 6 June 2022 for global solar irradiance (*GHI*), global ultraviolet irradiance (*GHUV*), air temperature (*T*), relative humidity (*RH*), and wind speed (*WS*), for overcast, intermediate, and clear sky conditions classified in accordance with the k_t criteria.

Sky Type	Parameter	All Data	Season			
			Winter	Spring	Summer	Autumn
All Sky	N	34,270	7,824	10,458	6,972	9,016
	GHI (W·m^{-2})	353.27	258.17	412.21	499.63	254.23
	GHUV (W·m^{-2})	13.33	9.36	15.83	19.09	9.41
	T (°C)	13.20	7.44	13.68	21.51	11.21
	RH (%)	67.96	75.31	65.40	54.82	74.72
	WS (m·s^{-1})	2.15	2.37	2.17	1.97	2.09

Table 5. *Cont.*

Sky Type	Parameter	All Data	Season			
			Winter	Spring	Summer	Autumn
Overcast skies ($0 \leq k_t \leq 0.35$)	N	11,971	3,281	3,584	1,314	3,792
	GHI ($W \cdot m^{-2}$)	120.31	108.32	142.60	140.64	102.56
	GHUV ($W \cdot m^{-2}$)	5.51	4.86	6.54	6.60	4.73
	T (°C)	9.87	6.10	11.24	17.33	9.24
	RH (%)	82.41	85.64	79.15	71.97	86.30
	WS ($m \cdot s^{-1}$)	2.26	2.53	2.15	1.74	2.31
Intermediate skies ($0.35 < k_t \leq 0.65$)	N	9,579	2,240	2,916	1,885	2,538
	GHI ($W \cdot m^{-2}$)	312.54	278.81	361.07	335.61	269.44
	GHUV ($W \cdot m^{-2}$)	12.08	10.43	14.22	13.20	10.25
	T (°C)	12.97	7.75	13.78	20.27	11.24
	RH (%)	68.20	74.07	64.99	59.38	73.27
	WS ($m \cdot s^{-1}$)	2.11	2.43	2.09	1.83	2.05
Clear skies ($0.65 < k_t \leq 1$)	N	12,720	2,303	3,958	3,773	2,686
	GHI ($W \cdot m^{-2}$)	603.17	451.58	694.03	706.59	454.00
	GHUV ($W \cdot m^{-2}$)	21.63	14.75	25.43	26.40	15.22
	T (°C)	16.51	9.05	15.83	23.59	13.97
	RH (%)	54.18	61.80	53.24	46.56	59.74
	WS ($m \cdot s^{-1}$)	2.08	2.08	2.24	2.11	1.82

3. Results and Discussion

3.1. Sky Classification

Definition of (clear, intermediate, and overcast) sky types is usually achieved through meteorological and climate indices. Among others, the clearness index, k_t (ratio of global solar irradiation to extraterrestrial solar irradiation) [67–70], relative sunshine, S, [71,72], Perez's clearness index, ε, and sky brightness, Δ, [73,74], have been proposed as sky type classifiers. A previous study concluded [66] that limited results for sky classification can be obtained using meteorological indices. In 2003, the CIE adopted 15 standard sky types (five clear, five intermediate, and five overcast skies) in order to create a standard for sky classification [61]; these were defined by the International Commission on Illumination (*Commission Internationale de L'Éclairage* or CIE), and each one was perfectly characterized in terms of energy and daylight, and widely considered as an adequate representation of empirical sky conditions [75–80]. Therefore, the CIE standard for sky taxonomy was selected as the reference for atmospheric conditions. A complete description of the CIE standard sky classification model and the procedure for obtaining a CIE standard sky classification from sky scanner measurements can be found in previous works [62,63,81,82].

Figure 2 shows the frequency of occurrence of each CIE standard sky type in Burgos, Spain, during the experimental campaign. Skies in Burgos are predominantly clear, the most frequent sky type in the city being CIE standard sky type 13 (cloudless polluted with a broader solar corona), with a Frequency of Occurrence (FOC) higher than 18%. As can be observed in Figure 3, the fifteen CIE categories are grouped into overcast (CIE categories 1 to 5), partly cloudy (6 to 10), and clear skies (11 to 15); the clear sky conditions have the highest FOC (44.63%). This result concurs with previous experimental campaigns developed in Burgos between 2016 and 2022 [82,83]. As CIE standard sky classification data around the world are quite scarce, an alternative sky classification model, based on the k_t classification, was prepared. A comparison with CIE taxonomy is shown in Figure 3.

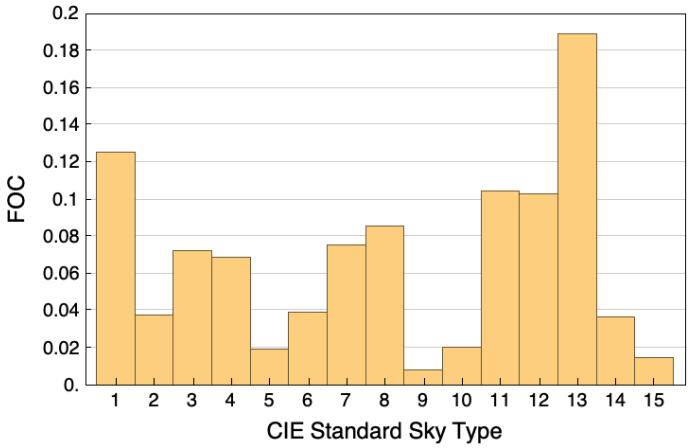

Figure 2. Frequency of Occurrence (FOC) of each CIE standard sky type in Burgos (Spain) from 14 September 2020 to 6 June 2022.

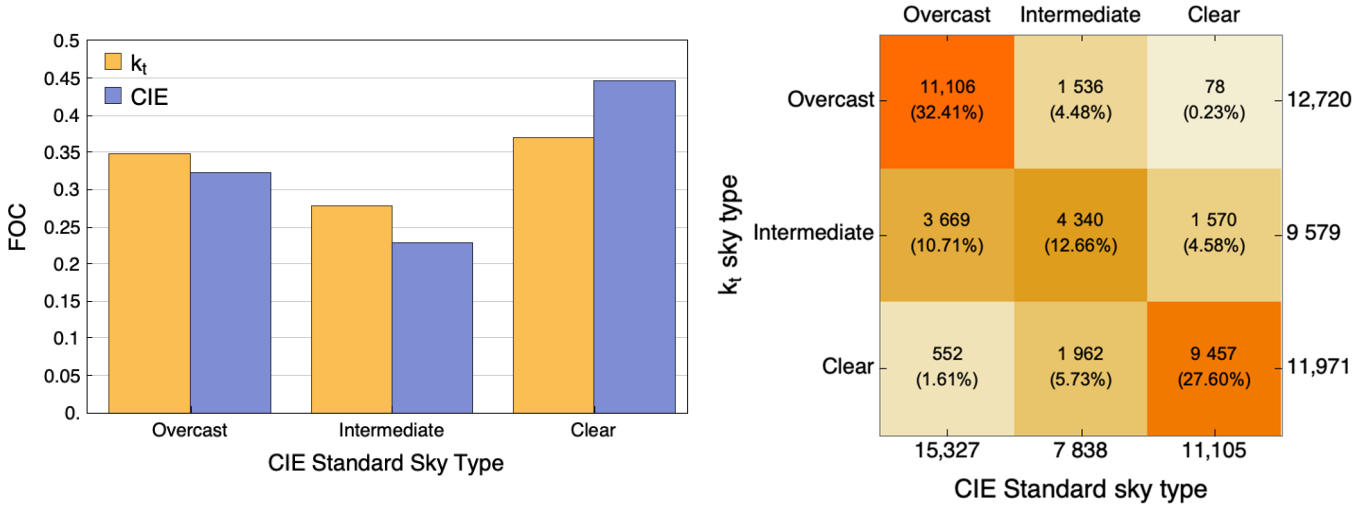

(**a**) (**b**)

Figure 3. (**a**) Frequency of occurrence (FOC) of the CIE and k_t sky classifications in Burgos (Spain) from 14 September 2020 to 6 June 2022; and (**b**) confusion matrix showing the coincidences in the classifications obtained according to both criteria.

The number of experimental data classified in each sky type category is shown in Figure 3a. The CIE classifies sky conditions as being clear more frequently than k_t, and as overcast or an intermediate sky type less frequently than k_t. The number of classification matches obtained, according to the CIE and k_t classifications, can be seen in the confusion matrix in Figure 3b.

k_t is closely linked to the irradiance value [1], whereas the CIE classification considers the angular distribution of sky radiance and luminance. In this sense, some of the CIE sky types included in the clear category are described as skies with a certain degree of turbidity or pollution, such as CIE sky type 13 (cloudless polluted with a broader solar corona), CIE sky type 14 (cloudless turbid with a broader solar corona), and CIE sky type 15 (white-blue turbid sky with a wide solar corona effect). This is linked to relatively low k_t values [66]. In any case, there is good agreement between the two classification criteria, as can be seen in Figure 3b.

3.2. Analysis of the 10 min GHUV/GHI Ratio

Figure 4 shows the evolution of the 10 min values of *GHUV*, *GHI*, and its ratio (*GHUV/GHI*), which were measured in Burgos throughout the experimental campaign. It should be noted that the gray areas that appear in the three plots in Figure 4, for each day between sunrise and sunset, correspond to missing data, either because they were not recorded or because they did not pass the QC described in Section 2. With regard to Figure 4c, the *GHUV/GHI* ratios assume values between 1% and 10%; however, the highest values are clearly concentrated in the early hours of the day, and they decrease significantly during the central hours, although there is no clear trend throughout the day. This evolution is analyzed in detail in Section 3.3.

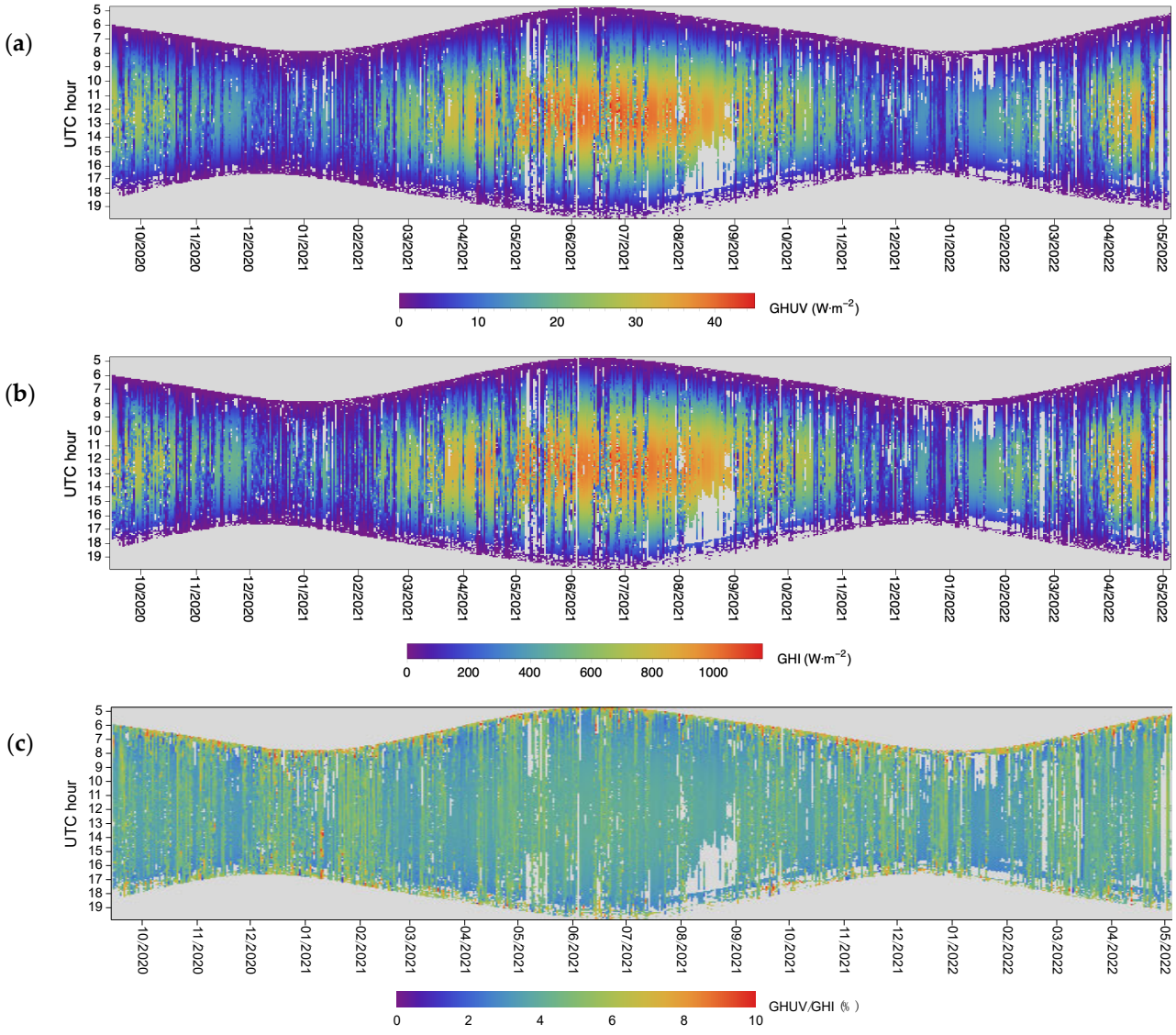

Figure 4. Ten minute experimental data of (**a**) *GHUV* (W·m^{-2}), (**b**) *GHI* (W·m^{-2}), and (**c**) the *GHUV/GHI* ratio (%) throughout the experimental campaign.

Although the scale used to represent the *GHUV/GHI* ratio values in Figure 4c reaches up to 10%, there are some values that considerably exceed this threshold (up to 15.21%): however, as can be seen in Figure 5a, which shows the Cumulative Distribution Function (CDF) of the 10 min *GHUV/GHI* ratios, the probability of this ratio exceeding 10% is extremely low (less than 0.05%). Figure 5a also shows the good fit between the empirical CDF (blue line) and the CDF adjusted to a normal distribution function (yellow line).

This can also be seen in Figure 5b, which shows the empirical Probability Distribution Function (PDF) of the 10 min *GHUV/GHI* ratios, and the adjusted PDF that shows a normal distribution.

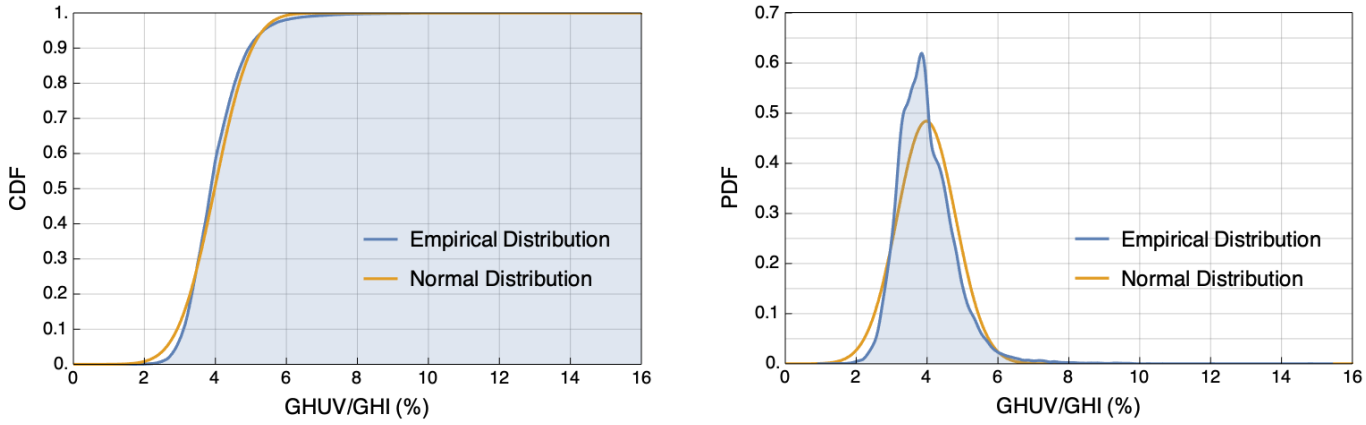

(**a**) (**b**)

Figure 5. Cumulative distribution function (**a**) and probability distribution function (**b**) of the 10 min data measured during the experimental campaign. Both the empirical CDF and PDF (blue line), and the CDF and PDF that were adjusted to a normal distribution function (yellow line), are plotted.

3.3. Hourly, Monthly, and Seasonal Analysis of the GHUV/GHI Ratio

Figure 6 shows the boxplot of the mean hourly values of the *GHUV/GHI* ratio, calculated from the average of the 10 min data, from sunrise to sunset, using the whole database. The graph represents the mean value (gray crosses), the median (white lines), the three quartiles, and both the maximum and minimum data values, as well as the outlier values. The mean hourly value of *GHUV/GHI* remained almost constant throughout the day. As previously noted, a small increase can be seen in the early hours of the day, which tends to stabilize during the central hours, and increases again at sunset. As the interquartile range shows, a greater dispersion of values in the first and last hours (1.9% at 5:00 h and 19:00 h), than in the central hours (0.75% at 12:00 h), of the day is observable. The average values were higher than the median values across all hours of the day. The hourly average of the ratio was 3.98 ± 0.82%, with maximum and minimum values of 4.25 ± 1.49% and 3.80 ± 1.14%, at 19:00 and at 18:00 h, respectively. These data, shown in Table 1, are comparable with other data from different locations in Spain. The hourly *GHUV/GHI* ratio in Burgos is higher than the ratio recorded at Almería (3.7%) [53], and lower than the ratios recorded at Granada (4%) [53], Valladolid (4.1%) [22], Valencia (4.2%), and Cordoba (4.9%) [23]; this is mainly due to each location's different sky conditions and their various heights above sea level.

Figures 7 and 8 show the statistical analysis of the monthly and seasonal averages of the *GHUV/GHI* ratio, which was calculated using the averages of the 10 min dataset, using the whole database. Figure 7 shows that the monthly data were almost constant throughout the year, with a small decrease in July and August. The standard deviation fluctuated between 0.69 and 1.23%, and the interquartile range was between 0.44% and 1.56%. December and January were the measurement campaign months with the highest data dispersion: the interquartile ranges were 1.51% and 1.56% with standard deviations of 1.29% and 1.27%, respectively. The maximum value was recorded in December (4.35% ± 1.29%), whereas the minimum was reached in July (3.82% ± 0.69%). A greater dispersion of values is observable in Figure 8 for the winter and autumn months, whereas the values in the summer months were closer, and therefore, they presented a smaller dispersion. These results are similar to the results obtained at other locations around the world (see Table 1), and the main differences between them can be attributed to the specific sky conditions, rather than the temporal variability of the ratio.

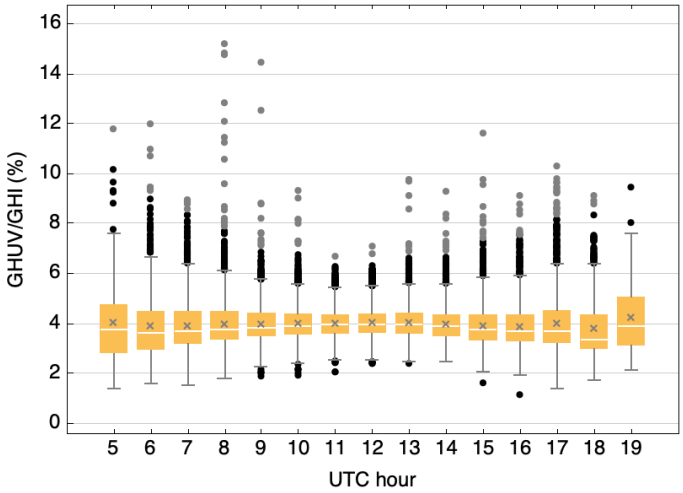

Figure 6. Boxplot of the *GHUV/GHI* hourly averages using the 10 min data. Gray crosses indicate the mean, and the white lines inside the box indicate the median. The limits of the boxes define the first, second, and third quartiles, whereas the extreme whiskers show the minimum and the maximum points. Black and gray circles represent outliers.

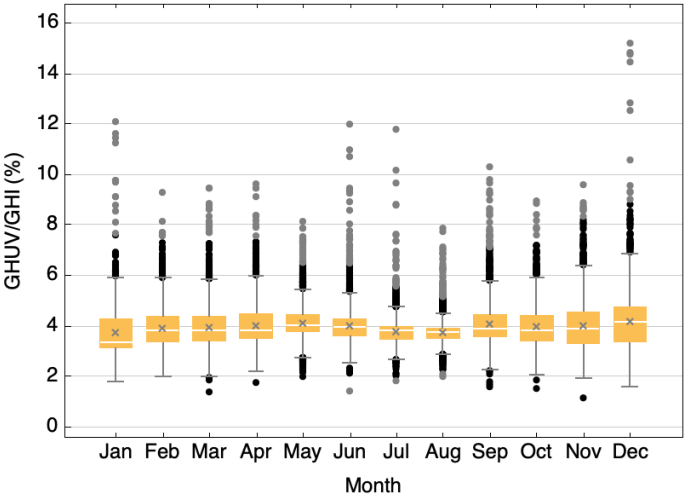

Figure 7. Boxplot of the *GHUV/GHI* monthly averages based on 10 min datasets.

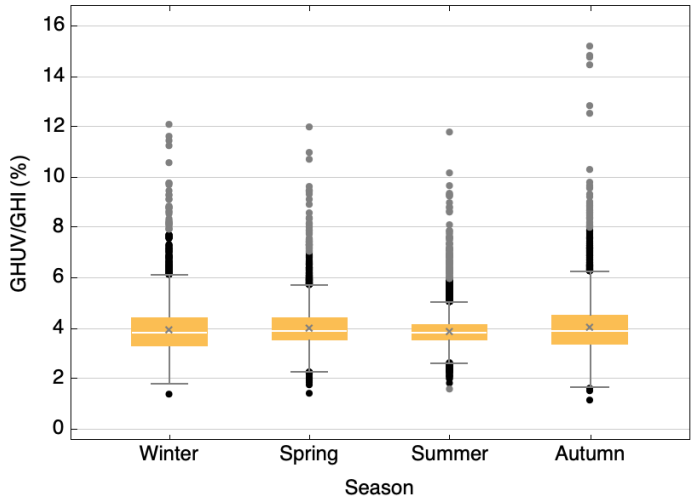

Figure 8. Boxplot of the *GHUV/GHI* seasonal averages based on the 10 min datasets.

3.4. GHUV/GHI Ratio and Sky Conditions

As explained in Section 3.1, during the experimental campaign, sky conditions were determined in Burgos using the CIE standard sky classification, or alternatively, the k_t criteria. Figure 9 shows the results of the statistical analysis of the average *GHUV/GHI* ratio, calculated using 10 min intervals, for each CIE standard sky type. The highest ratio values were obtained for sky types 5 (4.85 ± 0.92%) and 1 (4.73 ± 0.76%), which corresponded with the overcast sky conditions.

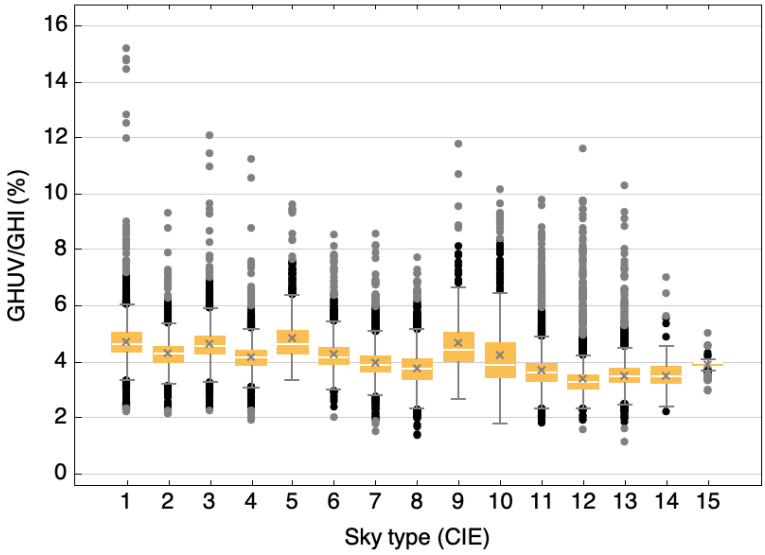

Figure 9. Boxplot of the average *GHUV/GHI* ratios for each CIE sky type using the 10 min data.

Figure 10 presents a comparison of the statistical analyses of the aggregated CIE sky types and the data classifications according to k_t. The same trend can be observed in both cases (i.e., the *GHUV/GHI* ratio was higher for overcast skies and lower for clearer skies). The mean values obtained in both cases, as well as their dispersion values, were similar; they were slightly higher for the overcast and intermediate sky types that were classified using the k_t taxonomy, and the results for the clear sky type were similar, as Table 6 shows.

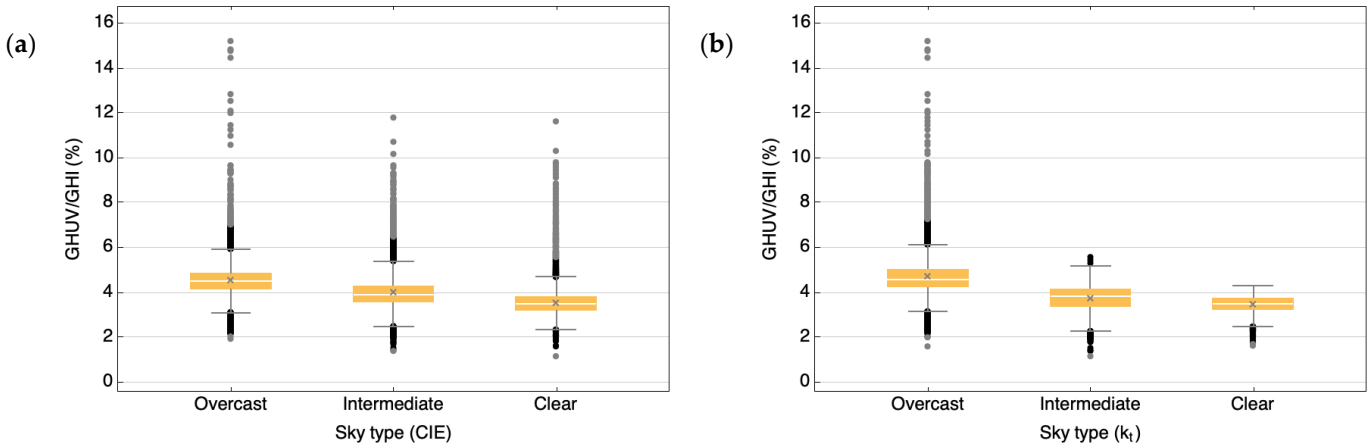

Figure 10. Boxplot of the *GHUV/GHI* average values for (**a**) each CIE sky type group and (**b**) for each sky type classification according to k_t, based on the 10 min datasets.

Table 6. Mean, standard deviation (STD), and interquartile range (IQR) of the *GHUV/GHI* average values (%), based on the 10 min datasets for clear, intermediate, and overcast sky types, which were classified according to the k_t and CIE criteria.

	Mean (%)		**STD (%)**		**IQR (%)**	
Sky classification	k_t	CIE	k_t	CIE	k_t	CIE
Overcast	4.719	4.562	0.844	0.737	0.751	0.711
Intermediate	3.740	4.007	0.542	0.780	0.745	0.725
Clear	3.469	3.547	0.350	0.619	0.507	0.589

The main characteristics of the monthly and seasonal *GHUV* and *GHI* ratios, based on the 10 min, hourly, and daily averages, were studied. The linear trend lines of both formulations ($GHUV = a{\cdot}GHI + b$, and $GHUV = a{\cdot}GHI$) were employed. According to several works, the formulation of the equation affects the quality of the results, due to errors induced by forcing the intercept to zero [34]. The temporal changes were examined, together with the effect of cloudiness; therefore, the k_t cloudiness classification was used to characterize the sky conditions. The results of these studies are depicted in Tables 7–9.

Table 7. Monthly, seasonal, and total averages of the *GHUV/GHI* ratio, number of 10 min values (N) and standard deviations (SD) under different sky conditions, together with the slope (a), offset (b), and R^2 values of the linear regressions $GHUV = a{\cdot}GHI + b$ and $GHUV = a{\cdot}GHI$.

Month/ Season	**All Skies**								**Overcast Skies(k_t<0.35)**			**Intermediate Skies(0.35≤k_t≤0.65)**			**Clear Skies(k_t>0.65)**		
	Σ(GHUV/GHI)/N			***GHUV=a·GHRa+b***			***GHUV=a·GHRa***		**Σ(GHUV/GHI)/N**			**Σ(GHUV/GHI)/N**			**Σ(GHUV/GHI)/N**		
	Value	***SD***	***N***	***a***	***b***	R^2	***a***	R^2	**Value**	***SD***	***N***	**Value**	***SD***	***N***	**Value**	***SD***	***N***
January	0.0375	0.0096	2026	0.0301	1.0802	0.9548	0.0331	0.9868	0.0477	0.0100	640	0.0365	0.0057	411	0.0312	0.0022	975
February	0.0393	0.0077	2862	0.0328	0.9594	0.9673	0.0352	0.9883	0.0461	0.0069	1132	0.0369	0.0045	943	0.0325	0.0026	787
March	0.0394	0.0080	3830	0.0341	0.9029	0.9689	0.0359	0.9885	0.0448	0.0082	1678	0.0367	0.0056	1107	0.0335	0.0027	1045
April	0.0401	0.0077	4213	0.0361	0.7294	0.9750	0.0373	0.9917	0.0473	0.0071	1509	0.0377	0.0054	1115	0.0349	0.0031	1589
May	0.0413	0.0072	3213	0.0383	0.5646	0.9831	0.0392	0.9938	0.0471	0.0072	1179	0.0388	0.0054	1073	0.0369	0.0032	961
June	0.0402	0.0078	2381	0.0392	−0.0572	0.9833	0.0391	0.9951	0.0487	0.0102	559	0.0384	0.0062	554	0.0372	0.0030	1268
July	0.0380	0.0063	2459	0.0394	−0.7329	0.9844	0.0384	0.9959	0.0477	0.0097	302	0.0364	0.0061	602	0.0367	0.0031	1555
August	0.0376	0.0057	1865	0.0383	−0.4667	0.9845	0.0376	0.9962	0.0468	0.0082	226	0.0356	0.0057	443	0.0365	0.0027	1196
September	0.0409	0.0084	3023	0.0362	0.8783	0.9697	0.0378	0.9907	0.0488	0.0092	973	0.0388	0.0051	1026	0.0354	0.0029	1024
October	0.0399	0.0080	2983	0.0340	0.8853	0.9682	0.0360	0.9891	0.0470	0.0073	1154	0.0377	0.0051	831	0.0335	0.0025	998
November	0.0401	0.0090	2993	0.0312	1.1881	0.9475	0.0348	0.9815	0.0474	0.0077	1336	0.0369	0.0050	785	0.0317	0.0023	872
December	0.0420	0.0112	2422	0.0303	1.1408	0.9383	0.0348	0.9747	0.0490	0.0105	1283	0.0363	0.0049	689	0.0309	0.0025	450
Winter	0.0394	0.0088	7824	0.0327	0.9126	0.9557	0.0351	0.9845	0.0463	0.0086	3281	0.0368	0.0052	2240	0.0320	0.0026	2303
Spring	0.0402	0.0076	10,458	0.0373	0.4694	0.9772	0.0380	0.9923	0.0471	0.0077	3584	0.0379	0.0055	2916	0.0358	0.0033	3958
Summer	0.0390	0.0069	6972	0.0383	−0.0557	0.9812	0.0382	0.9949	0.0480	0.0088	1314	0.0374	0.0059	1885	0.0366	0.0029	3773
Autumn	0.0404	0.0092	9016	0.0338	0.8111	0.9615	0.0359	0.9859	0.0478	0.0088	3792	0.0373	0.0051	2538	0.0327	0.0028	2686
All data	0.0398	0.0082	34,270	0.0370	0.2455	0.9746	0.0375	0.9907	0.0472	0.0084	11,971	0.0374	0.0054	9579	0.0347	0.0035	12,720

Table 8. Monthly, seasonal, and total *GHUV/GHI* average values, number of hourly values (N) and standard deviations (SD) under different sky conditions, together with the slope (a), offset (b), and R^2 values of the linear regressions $GHUV = a{\cdot}GHI + b$ and $GHUV = a{\cdot}GHI$.

Month/ Season	**All Skies**								**Overcast Skies(k_t<0.35)**			**Intermediate Skies(0.35≤k_t≤0.65)**			**Clear Skies(k_t>0.65)**		
	Σ(GHUV/GHI)/N			***GHUV=a·GHRa+b***			***GHUV=a·GHRa***		**Σ(GHUV/GHI)/N**			**Σ(GHUV/GHI)/N**			**Σ(GHUV/GHI)/N**		
	Value	***SD***	***N***	***a***	***b***	R^2	***a***	R^2	**Value**	***SD***	***N***	**Value**	***SD***	***N***	**Value**	***SD***	***N***
January	0.0420	0.0133	632	0.0316	0.6390	0.9702	0.0336	0.9858	0.0512	0.0124	255	0.0391	0.0109	176	0.0331	0.0079	201
February	0.0400	0.0089	591	0.0339	0.5703	0.9776	0.0354	0.9907	0.0466	0.0089	237	0.0373	0.0060	223	0.0329	0.0033	131
March	0.0410	0.0103	786	0.0350	0.5476	0.9777	0.0362	0.9902	0.0458	0.0111	345	0.0380	0.0075	270	0.0358	0.0077	171
April	0.0409	0.0096	827	0.0368	0.3907	0.9831	0.0375	0.9934	0.0480	0.0105	290	0.0377	0.0057	270	0.0364	0.0070	267
May	0.0425	0.0100	735	0.0390	0.3015	0.9882	0.0395	0.9948	0.0485	0.0110	265	0.0394	0.0079	299	0.0386	0.0069	171
June	0.0413	0.0099	477	0.0396	−0.1978	0.9904	0.0393	0.9963	0.0510	0.0134	116	0.0384	0.0072	157	0.0381	0.0042	204
July	0.0390	0.0092	474	0.0393	−0.6195	0.9902	0.0385	0.9966	0.0504	0.0156	68	0.0370	0.0083	144	0.0371	0.0034	262
August	0.0379	0.0064	399	0.0383	−0.4445	0.9900	0.0377	0.9966	0.0469	0.0087	57	0.0357	0.0059	120	0.0367	0.0032	222
September	0.0409	0.0086	592	0.0374	0.3882	0.9825	0.0382	0.9940	0.0474	0.0102	179	0.0391	0.0064	251	0.0363	0.0044	162
October	0.0411	0.0105	739	0.0350	0.4568	0.9823	0.0361	0.9928	0.0492	0.0114	264	0.0386	0.0077	246	0.0345	0.0044	229
November	0.0407	0.0097	605	0.0329	0.7094	0.9672	0.0352	0.9863	0.0474	0.0087	263	0.0376	0.0075	205	0.0326	0.0048	137
December	0.0433	0.0125	614	0.0324	0.6349	0.9635	0.0351	0.9813	0.0503	0.0117	314	0.0370	0.0066	198	0.0339	0.0109	102
Winter	0.0418	0.0117	1933	0.0338	0.5313	0.9695	0.0353	0.9862	0.0486	0.0117	848	0.0383	0.0084	644	0.0338	0.0075	441
Spring	0.0412	0.0097	2164	0.0379	0.2326	0.9843	0.0383	0.9936	0.0480	0.0108	744	0.0382	0.0069	756	0.0371	0.0064	664
Summer	0.0396	0.0086	1396	0.0387	−0.2087	0.9883	0.0384	0.9960	0.0489	0.0124	275	0.0377	0.0072	471	0.0371	0.0035	650
Autumn	0.0411	0.0104	1978	0.0350	0.4390	0.9776	0.0361	0.9903	0.0485	0.0103	786	0.0379	0.0071	688	0.0339	0.0061	504
All data	0.0410	0.0102	7471	0.0375	0.0857	0.9827	0.0376	0.9923	0.0484	0.0111	2653	0.0381	0.0074	2559	0.0358	0.0061	2259

Table 9. Monthly, seasonal, and total *GHUV/GHI* average values, number of daily values (N) and standard deviations (SD) under different sky conditions, together with the slope (a), offset (b), and R^2 values of the linear regressions $GHUV = a{\cdot}GHI + b$ and $GHUV = a{\cdot}GHI$.

Month/ Season	All Skies								Overcast Skies(k_t<0.35)			Intermediate Skies(0.35≤k_t≤0.65)			Clear Skies(k_t>0.65)		
	Σ(GHUV/GHI)/N			*GHUV=a·GHRa+b*			*GHUV=a·GHRa*		Σ(GHUV/GHI)/N			Σ(GHUV/GHI)/N			Σ(GHUV/GHI)/N		
	Value	*SD*	*N*	*a*	*b*	R^2	*a*	R^2	Value	*SD*	*N*	Value	*SD*	*N*	Value	*SD*	*N*
January	0.0376	0.0061	62	0.0271	1.7037	0.9851	0.0335	0.9897	0.0447	0.0043	19	0.0367	0.0038	24	0.0318	0.0007	19
February	0.0375	0.0043	56	0.0306	1.3763	0.9765	0.0354	0.9944	0.0432	0.0036	14	0.0361	0.0025	36	0.0330	0.0007	6
March	0.0382	0.0048	62	0.0314	1.6457	0.9663	0.0362	0.9929	0.0422	0.0050	20	0.0368	0.0034	31	0.0349	0.0026	11
April	0.0391	0.0039	60	0.0325	1.9853	0.9842	0.0371	0.9959	0.0438	0.0028	19	0.0377	0.0021	23	0.0358	0.0009	18
May	0.0398	0.0046	62	0.0380	0.4841	0.9907	0.0391	0.9975	0.0451	0.0039	15	0.0382	0.0036	39	0.0379	0.0010	8
June	0.0386	0.0038	34	0.0376	0.6227	0.9938	0.0388	0.9988	0.0421	0.0035	5	0.0378	0.0051	15	0.0381	0.0005	14
July	0.0383	0.0016	31	0.0334	2.4846	0.9712	0.0379	0.9989	-	-	0	0.0392	0.0020	13	0.0376	0.0007	18
August	0.0374	0.0014	31	0.0353	1.0985	0.9540	0.0373	0.9990	-	-	0	0.0376	0.0016	19	0.0372	0.0010	12
September	0.0392	0.0025	47	0.0325	2.1721	0.9736	0.0381	0.9966	0.0427	0.0015	8	0.0390	0.0018	32	0.0359	0.0013	7
October	0.0383	0.0044	62	0.0313	1.6001	0.9835	0.0359	0.9954	0.0442	0.0044	15	0.0373	0.0021	33	0.0343	0.0011	14
November	0.0383	0.0048	60	0.0279	1.7580	0.9734	0.0353	0.9903	0.0432	0.0031	22	0.0364	0.0025	29	0.0323	0.0012	9
December	0.0398	0.0055	62	0.0284	1.3206	0.9830	0.0353	0.9876	0.0442	0.0033	27	0.0371	0.0034	27	0.0338	0.0061	8
Winter	0.0382	0.0055	179	0.0302	1.3644	0.9613	0.0351	0.9900	0.0438	0.0044	59	0.0366	0.0035	88	0.0326	0.0021	32
Spring	0.0389	0.0042	168	0.0358	0.9105	0.9810	0.0379	0.9960	0.0438	0.0034	41	0.0378	0.0035	86	0.0365	0.0016	41
Summer	0.0386	0.0021	100	0.0342	1.9054	0.9811	0.0379	0.9984	0.0430	0.0014	8	0.0387	0.0019	53	0.0375	0.0008	39
Autumn	0.0385	0.0046	182	0.0325	1.0597	0.9721	0.0360	0.9933	0.0436	0.0035	56	0.0371	0.0023	94	0.0338	0.0031	32
All data	0.0386	0.0045	629	0.0358	0.5145	0.9763	0.0372	0.9947	0.0437	0.0037	164	0.0374	0.0030	321	0.0353	0.0028	144

Figure 11 shows the high positive correlation between both magnitudes, at 10 min, hourly, and daily intervals. Better fitting was obtained using no intercept linear regression models rather than linear regression models with an intercept, and the R^2 statistic increased as the time intervals lengthened; however, as is evident, both regressions were very similar. No significant differences were found for the slope and standard deviation values of the fitted data for the different considered time intervals.

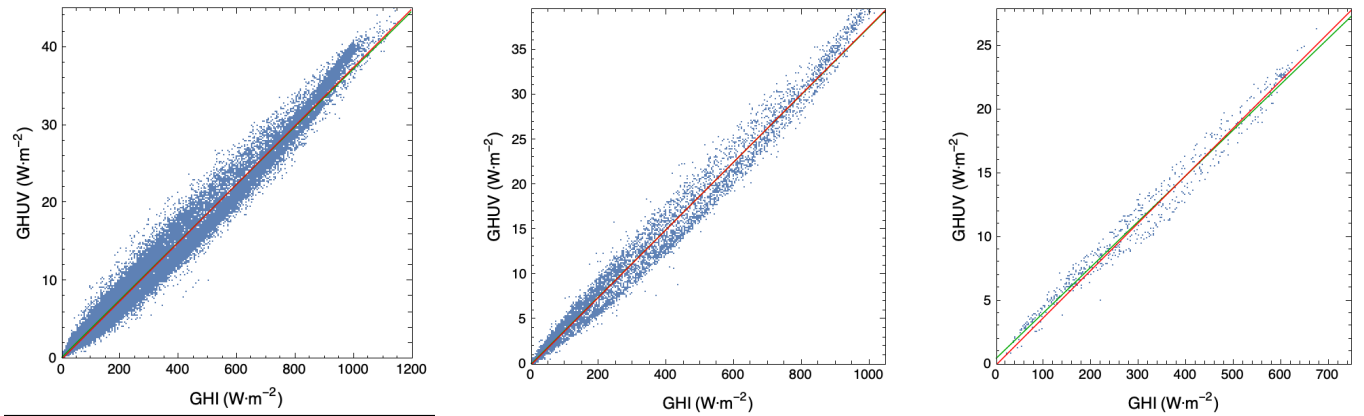

(**a**) (**b**) (**c**)

Figure 11. *GHUV* and *GHI* (W·m^{-2}) values recorded in Burgos (Spain) from 14 September 2020 to 6 June 2022: (**a**) 10 min data; (**b**) hourly average of 10 min data; (**c**) daily average of 10 min data. Tables below each plot show the two linear regressions (with and without constant), as well as the R^2 value and the 95% confidence interval (CI).

4. Conclusions

High quality *GHUV* and *GHI* datasets were recorded at 10 min intervals and analyzed in Burgos, Spain, between September 2020 and June 2022. The analysis of the experimental data has shown a representative dependency on the sky type conditions, classified with both the CIE and k_t taxonomies. The *GHUV/GHI* ratio yielded higher values for overcast sky types, and lower values with a higher scatter under clear sky conditions. A global

review of some *GHUV/GHI* ratios around the world has shown that *GHUV*, regardless of the temporal basis of the recorded data, accounts for up to 4% of the total incidence of *GHI* measured at the same location; the location's height above sea level and the sky conditions were the most influential parameters for the absolute value of the ratio. The value of the ratio increased in the categories which represented cloudier skies.

During this exhaustive analysis, the ratio did not exhibit any seasonal, monthly, or daily dependency, other than the predominance of one type of sky over another, in the period being analyzed.

Slight differences in the value of the ratio (mean and standard deviation) were detected depending on the sky classification criteria that was being used; the main difference between the values was the number of data that were classified as outliers. The fact that there was a higher number of outliers that corresponded with the CIE clear skies categories could be explained by the presence of aerosols or atmospheric turbidity; these factors are characteristic of clear sky types 13, 14, and 15, with a FOC of 19%, 3.8%, and 1.6% respectively.

The main conclusion, for practical purposes, is that the proportional relation between *GHUV* and *GHI* can be used for modelling *GHUV*.

Author Contributions: S.G.-R.: methodology, software, formal analysis, investigation, visualization. I.G.: methodology, software, formal analysis, investigation, original draft preparation, writing-review and editing, visualization; A.G.-R.: methodology, software, visualization; M.D.-M.: conceptualization, validation, original draft preparation, supervision, project administration; C.A.-T.: conceptualization, writing—review and editing; supervision, funding acquisition. All authors have read and agreed to the published version of the manuscript.

Funding: This research was funded by the Spanish Ministry of Science and Innovation, grant numbers RTI2018-098900-B-I00 and TED2021-131563B-I00, and Junta de Castilla y León, grant numbers INVESTUN/19/BU/0004 and INVESTUN/22/BU/0001.

Institutional Review Board Statement: Not applicable.

Informed Consent Statement: Not applicable.

Data Availability Statement: Copies of the original dataset used in this work can be downloaded from https://riubu.ubu.es/handle/10259/5512 (accessed on 10 October 2022).

Acknowledgments: Ignacio Garcia thanks the Spanish Ministry of Universities and the European Union-Next Generation EU for their financial support (program for the requalification of the Spanish university system 2021–2023, Resolution 14 February 2021).

Conflicts of Interest: The authors declare no conflict of interest.

References

1. Iqbal, M. *An Introduction to Solar Radiation*; Academic Press: Cambridge, MA, USA, 1983.
2. Soueid, L.; Triguero-Mas, M.; Dalmau, A.; Barrera-Gómez, J.; Alonso, L.; Basagaña, X.; Thieden, E.; Wulf, H.C.; Diffey, B.; Young, A.R.; et al. Estimating personal solar ultraviolet radiation exposure through time spent outdoors, ambient levels and modelling approaches*. *Br. J. Dermatol.* **2022**, *186*, 266–273. [CrossRef] [PubMed]
3. Vuilleumier, L.; Harris, T.; Nenes, A.; Backes, C.; Vernez, D. Developing a UV climatology for public health purposes using satellite data. *Environ. Int.* **2021**, *146*, 106177. [CrossRef] [PubMed]
4. Heisler, G.M.; Grant, R.H. Ultraviolet radiation in urban ecosystems with consideration of effects on human health. *Urban Ecosyst.* **2000**, *4*, 193–229. [CrossRef]
5. Ndiaye, A.; Charki, A.; Kobi, A.; Kébé, C.M.F.; Ndiaye, P.A.; Sambou, V. Degradations of silicon photovoltaic modules: A literature review. *Sol. Energy* **2013**, *96*, 140–151. [CrossRef]
6. Zhang, Y.; Kaiser, E.; Zhang, Y.; Zou, J.; Bian, Z.; Yang, Q.; Li, T. UVA radiation promotes tomato growth through morphological adaptation leading to increased light interception. *Environ. Exp. Bot.* **2020**, *176*, 104073. [CrossRef]
7. Häder, D.P.; Williamson, C.E.; Wängberg, S.Å.; Rautio, M.; Rose, K.C.; Gao, K.; Helbling, E.W.; Sinha, R.P.; Worrest, R. Effects of UV radiation on aquatic ecosystems and interactions with other environmental factors. *Photochem. Photobiol. Sci.* **2015**, *14*, 108–126. [CrossRef]
8. Grant, W.B.; Boucher, B.J. An Exploration of How Solar Radiation Affects the Seasonal Variation of Human Mortality Rates and the Seasonal Variation in Some Other Common Disorders. *Nutrients* **2022**, *14*, 2519. [CrossRef]

9. Nandin de Carvalho, H. Latitude impact on pandemic SARS-CoV-2 2020 outbreaks and possible utility of UV indexes in predictions of regional daily infections and deaths. *J. Photochem. Photobiol.* **2022**, *10*, 100108. [CrossRef]
10. Nicastro, F.; Sironi, G.; Antonello, E.; Bianco, A.; Biasin, M.; Brucato, J.R.; Ermolli, I.; Pareschi, G.; Salvati, M.; Tozzi, P.; et al. Solar UV-B/A radiation is highly effective in inactivating SARS-CoV-2. *Sci. Rep.* **2021**, *11*, 14805. [CrossRef]
11. Porfirio, A.C.S.; De Souza, J.L.; Lyra, G.B.; Maringolo Lemes, M.A. An assessment of the global UV solar radiation under various sky conditions in Maceió-Northeastern Brazil. *Energy* **2012**, *44*, 584–592. [CrossRef]
12. Foyo-Moreno, I.; Alados, I.; Olmo, F.J.; Alados-Arboledas, L. The influence of cloudiness on UV global irradiance (295–385 nm). *Agric. For. Meteorol.* **2003**, *120*, 101–111. [CrossRef]
13. Wang, L.; Gong, W.; Lin, A.; Hu, B. Measurements and cloudiness influence on UV radiation in Central China. *Int. J. Climatol.* **2014**, *34*, 3417–3425. [CrossRef]
14. Mateos, D.; Román, R.; Bilbao, J.; de Miguel, A.; Pérez-Burgos, A. Cloud modulation of shortwave and ultraviolet solar irradiances at surface. *Opt. Pura Apl.* **2012**, *45*, 29–32. [CrossRef]
15. Ogunjobi, K.O.; Kim, Y.J. Ultraviolet (0.280–0.400 μm) and broadband solar hourly radiation at Kwangju, South Korea: Analysis of their correlation with aerosol optical depth and clearness index. *Atmos. Res.* **2004**, *71*, 193–214. [CrossRef]
16. Lerche, C.M.; Philipsen, P.A.; Wulf, H.C. UVR: Sun, lamps, pigmentation and vitamin D. *Photochem. Photobiol. Sci.* **2017**, *16*, 291–301. [CrossRef]
17. Wang, L.; Gong, W.; Li, J.; Ma, Y.; Hu, B. Empirical studies of cloud effects on ultraviolet radiation in Central China. *Int. J. Climatol.* **2014**, *34*, 2218–2228. [CrossRef]
18. Feng, L.; Wang, L.; Gong, W.; Lin, A.; Hu, B. Estimation of hourly and daily ultraviolet solar irradiation under various sky conditions at Sanya, Southern China. *Theor. Appl. Climatol.* **2015**, *121*, 187–198. [CrossRef]
19. Leal, S.S.; Tíba, C.; Piacentini, R. Daily UV radiation modeling with the usage of statistical correlations and artificial neural networks. *Renew. Energy* **2011**, *36*, 3337–3344. [CrossRef]
20. Al-Aruri, S.D. The empirical relationship between global radiation and global ultraviolet (0.290–0.385) μm solar radiation components. *Sol. Energy* **1990**, *45*, 61–64. [CrossRef]
21. Barbero, F.J.; López, G.; Batlles, F.J. Determination of daily solar ultraviolet radiation using statistical models and artificial neural networks. *Ann. Geophys.* **2006**, *24*, 2105–2114. [CrossRef]
22. Bilbao, J.; Mateos, D.; de Miguel, A. Analysis and cloudiness influence on UV total irradiation. *Int. J. Climatol.* **2011**, *31*, 451–460. [CrossRef]
23. Canada, J.; Pedros, G.; Bosca, J.V. Relationships between UV (0.290–0.385 μm) and broad band solar radiation hourly values in Valencia and Córdoba, Spain. *Energy* **2003**, *28*, 199–217. [CrossRef]
24. Escobedo, J.F.; Gomes, E.N.; Oliveira, A.P.; Soares, J. Modeling hourly and daily fractions of UV, PAR and NIR to global solar radiation under various sky conditions at Botucatu, Brazil. *Appl. Energy* **2009**, *86*, 299–309. [CrossRef]
25. Foyo-Moreno, I.; Vida, J.; Alados-Arboledas, L. Ground based ultraviolet (290–385 nm) and broadband solar radiation measurements in south-eastern Spain. *Int. J. Climatol.* **1998**, *18*, 1389–1400. [CrossRef]
26. Habte, A.; Sengupta, M.; Gueymard, C.A.; Narasappa, R.; Rosseler, O.; Burns, D.M. Estimating ultraviolet radiation from global horizontal irradiance. *IEEE J. Photovolt.* **2018**, *9*, 139–146. [CrossRef]
27. Jacovides, C.P.; Tymvios, F.S.; Asimakopoulos, D.N.; Kaltsounides, N.A.; Theoharatos, G.A.; Tsitouri, M. Solar global UVB (280–315nm) and UVA (315–380nm) radiant fluxes and their relationships with broadband global radiant flux at an eastern Mediterranean site. *Agric. For. Meteorol.* **2009**, *149*, 1188–1200. [CrossRef]
28. Lamy, K.; Portafaix, T.; Brogniez, C.; Godin-Beekmann, S.; Bencherif, H.; Morel, B.; Pazmino, A.; Metzger, J.M.; Auriol, F.; Deroo, C.; et al. Ultraviolet radiation modelling from ground-based and satellite measurements on Reunion Island, southern tropics. *Atmos. Chem. Phys.* **2018**, *18*, 227–246. [CrossRef]
29. Liu, H.; Hu, B.; Zhang, L.; Zhao, X.J.; Shang, K.Z.; Wang, Y.S.; Wang, J. Ultraviolet radiation over China: Spatial distribution and trends. *Renew. Sustain. Energy Rev.* **2017**, *76*, 1371–1383. [CrossRef]
30. Martinez-Lozano, J.A.; Tena, F.; Utrillas, M.P. Ratio of UV to global broad band irradiation in Valencia, Spain. *Int. J. Climatol.* **1999**, *19*, 903–911. [CrossRef]
31. Murillo, W.; Cañada, J.; Pedrós, G. Correlation between global ultraviolet (290-385nm) and global irradiation in Valencia and Cordoba (Spain). *Renew. Energy* **2003**, *28*, 409–418. [CrossRef]
32. Paulescu, M.; Stefu, N.; Tulcan-Paulescu, E.; Calinoiu, D.; Neculae, A.; Gravila, P. UV solar irradiance from broadband radiation and other meteorological data. *Atmos. Res.* **2010**, *96*, 141–148. [CrossRef]
33. Podstawczyńska, A. UV and global solar radiation in Łódź, Central Poland. *Int. J. Climatol. A J. R. Meteorol. Soc.* **2010**, *30*, 1–10.
34. Proutsos, N.; Alexandris, S.; Liakatas, A.; Nastos, P.; Tsiros, I.X. PAR and UVA composition of global solar radiation at a high altitude Mediterranean forest site. *Atmos. Res.* **2022**, *269*, 106039. [CrossRef]
35. Robaa, S.M. A study of ultraviolet solar radiation at Cairo urban area, Egypt. *Sol. Energy* **2004**, *77*, 251–259. [CrossRef]
36. Sahan, M. The measurements of the global solar radiation and solar ultraviolet radiation during 2018 year. In Proceedings of the Turkish Physical Society 35th International Physics Congress, TPS 2019, Bodrum, Turkey, 4–8 September 2019.
37. López, M.L.; Palancar, G.G.; Toselli, B.M. Effects of stratocumulus, cumulus, and cirrus clouds on the UV-B diffuse to global ratio: Experimental and modeling results. *J. Quant. Spectrosc. Radiat. Transf.* **2012**, *113*, 461–469. [CrossRef]

38. Calbó, J.; Pagès, D.; González, J.A. Empirical studies of cloud effects on UV radiation: A review. *Rev. Geophys.* **2005**, *43*, 1–28. [CrossRef]
39. Degünther, M.; Meerkötter, R. Effect of remote clouds on surface UV irradiance. In *Annales Geophysicae*; Springer: Berlin/Heidelberg, Germany, 2020; pp. 679–686.
40. Maghrabi, A.H.; Al-Dosari, A.F. Effects on surface meteorological parameters and radiation levels of a heavy dust storm occurred in Central Arabian Peninsula. *Atmos. Res.* **2016**, *182*, 30–35. [CrossRef]
41. Di Sarra, A.; Cacciani, M.; Chamard, P.; Cornwall, C.; Deluisi, J.J.; Di Iorio, T.; Disterhoft, P.; Fiocco, G.; Fuá, D.; Monteleone, F. Effects of desert dust and ozone on the ultraviolet irradiance: Observations at the Mediterranean island of Lampedusa during PAUR II. *J. Geophys. Res.* **2002**, *107*, PAU-2. [CrossRef]
42. Diffey, B.L. Sources and measurement of ultraviolet radiation. *Methods* **2002**, *28*, 4–13. [CrossRef]
43. Dvorkin, A.Y.; Steinberger, E.H. Modeling the altitude effect on solar UV radiation. *Sol. Energy* **1999**, *65*, 181–187. [CrossRef]
44. Singh, S.; Singh, R. High-altitude clear-sky direct solar ultraviolet irradiance at Leh and Hanle in the western Himalayas: Observations and model calculations. *J. Geophys. Res. D Atmos.* **2004**, *109*, D19201–D19212. [CrossRef]
45. Sola, Y.; Lorente, J.; Campmany, E.; de Cabo, X.; Bech, J.; Redaño, A.; Martínez-Lozano, J.A.; Utrillas, M.P.; Alados-Arboledas, L.; Olmo, F.J.; et al. Altitude effect in UV radiation during the Evaluation of the Effects of Elevation and Aerosols on the Ultraviolet Radiation 2002 (VELETA-2002) field campaign. *J. Geophys. Res. Atmos.* **2008**, *113*, D23. [CrossRef]
46. Baker-Blocker, A.; DeLuisi, J.J.; Dutton, E.G. Received ultraviolet radiation at the South Pole. *Sol. Energy* **1984**, *32*, 659–662. [CrossRef]
47. Al-Aruri, S.; Rasas, M.; Al-Jamal, K.; Shaban, N. An assessment of global ultraviolet solar radiation in the range (0.290–0.385 μm) in Kuwait. *Sol. Energy* **1988**, *41*, 159–162. [CrossRef]
48. Elhadidy, M.A.; Abdel-Nabi, D.Y.; Kruss, P.D. Ultraviolet solar radiation at Dhahran, Saudi Arabia. *Sol. Energy* **1990**, *44*, 315–319. [CrossRef]
49. Khogali, A.; Al-Bar, O.F. A study of solar ultraviolet radiation at Makkah solar station. *Sol. Energy* **1992**, *48*, 79–87. [CrossRef]
50. Feister, U.; Grasnick, K.H. Solar UV radiation measurements at Potsdam (52°22′ N, 13°5′ E). *Sol. Energy* **1992**, *49*, 541–548. [CrossRef]
51. Martinez-Lozano, J.A.; Casanovas, A.J.; Utrillas, M.P. Comparison of global ultraviolet (290–385 nm) and global irradiation measured during the warm season in valencia, spain. *Int. J. Climatol.* **1994**, *14*, 93–102. [CrossRef]
52. Shaltout, M.A.; Ghonim, M.M.; Trabea, A.A.; Allam, H. Ultraviolt solar radiation over Egypt. *Renew. Energy* **1994**, *5*, 1506–1508. [CrossRef]
53. Foyo-Moreno, I.; Vida, J.; Alados-Arboledas, L. A simple all weather model to estimate ultraviolet solar radiation (290–385 nm). *J. Appl. Meteorol.* **1999**, *38*, 1020–1026. [CrossRef]
54. Cañada, J.; Pedrós, G.; López, A.; Boscá, J.V. Influences of the clearness index for the whole spectrum and of the relative optical air mass on UV solar irradiance for two locations in the Mediterranean area, Valencia and Cordoba. *J. Geophys. Res. Atmos.* **2000**, *105*, 4759–4766. [CrossRef]
55. Koronakis, P.S.; Sfantos, G.K.; Paliatsos, A.G.; Kaldellis, J.K.; Garofalakis, J.E.; Koronaki, I.P. Interrelations of UV-global/global/diffuse solar irradiance components and UV-global attenuation on air pollution episode days in Athens, Greece. *Atmos. Environ.* **2002**, *36*, 3173–3181. [CrossRef]
56. Jacovides, C.P.; Assimakopoulos, V.D.; Tymvios, F.S.; Theophilou, K.; Asimakopoulos, D.N. Solar global UV (280–380 nm) radiation and its relationship with solar global radiation measured on the island of Cyprus. *Energy* **2006**, *31*, 2728–2738. [CrossRef]
57. Hu, B.; Wang, Y.; Liu, G. Influences of the clearness index on UV solar radiation for two locations in the Tibetan Plateau-Lhasa and Haibei. *Adv. Atmos. Sci.* **2008**, *25*, 885–896. [CrossRef]
58. Escobedo, J.F.; Gomes, E.N.; Oliveira, A.P.; Soares, J. Ratios of UV, PAR and NIR components to global solar radiation measured at Botucatu site in Brazil. *Renew. Energy* **2011**, *36*, 169–178. [CrossRef]
59. Escobedo, J.F.; Dal Pai, A.; de Oliveira, A.P.; Soares, J.; Dal Pai, E. Diurnal and Annual Evolution of UV, PAR and NIR Irradiations in Botucatu/Brazil. *Energy Procedia* **2014**, *57*, 1130–1139. [CrossRef]
60. Wang, L.; Gong, W.; Ma, Y.; Hu, B.; Wang, W.; Zhang, M. Analysis of ultraviolet radiation in Central China from observation and estimation. *Energy* **2013**, *59*, 764–774. [CrossRef]
61. *ISO 15469:2004(E)/CIE S 011/E:2003*; Spatial Distribution of Daylight—CIE Standard General Sky. ISO: Geneva, Switzerland; CIE: Vienna, Austria, 2004.
62. García-Rodríguez, A.; García-Rodríguez, S.; Granados-López, D.; Díez-Mediavilla, M.; Alonso-Tristán, C. Extension of PAR Models under Local All-Sky Conditions to Different Climatic Zones. *Appl. Sci.* **2022**, *12*, 2372. [CrossRef]
63. Granados-López, D.; Suárez-García, A.; Díez-Mediavilla, M.; Alonso-Tristán, C. Feature selection for CIE standard sky classification. *Sol. Energy* **2021**, *218*, 95–107. [CrossRef]
64. Hoyer-Klick, C.; Schillings, C.; Schroedter Homscheidt, M.; Beyer, H.G.; Dumortier, D.; Wald, L.; Ménard, L.; Gschwind, B.; Martinoli, M.; Gaboardi, E.; et al. Management and exploitation of solar resource knowledge. In Proceedings of the EUROSUN 2008, 1st International Congress on Heating, Cooling and Buildings, Lisbonne, Portugal, 7 October 2008; p. 405.
65. Gueymard, C.A. Revised composite extraterrestrial spectrum based on recent solar irradiance observations. *Sol. Energy* **2018**, *169*, 434–440. [CrossRef]

66. Suárez-García, A.; Díez-Mediavilla, M.; Granados-López, D.; González-Peña, D.; Alonso-Tristán, C. Benchmarking of meteorological indices for sky cloudiness classification. *J. Sol. Energy* **2020**, *195*, 499–513. [CrossRef]
67. Al-Shooshan, A.A. Estimation of photosynthetically active radiation under an arid climate. *J. Agric. Eng. Res.* **1997**, *66*, 9–13. [CrossRef]
68. Finch, D.A.; Bailey, W.G.; McArthur, L.J.B.; Nasitwitwi, M. Photosynthetically active radiation regimes in a southern African savanna environment. *Agric. For. Meteorol.* **2004**, *122*, 229–238. [CrossRef]
69. Jacovides, C.P.; Tymvios, F.S.; Assimakopoulos, V.D.; Kaltsounides, N.A. The dependence of global and diffuse PAR radiation components on sky conditions at Athens, Greece. *Agric. For. Meteorol.* **2007**, *143*, 277–287. [CrossRef]
70. Wang, L.; Gong, W.; Lin, A.; Hu, B. Analysis of photosynthetically active radiation under various sky conditions in Wuhan, Central China. *Int. J. Biometeorol.* **2014**, *58*, 1711–1720. [CrossRef]
71. Udo, S.O.; Aro, T.O. Global PAR related to global solar radiation for central Nigeria. *Agric. For. Meteorol.* **1999**, *97*, 21–31. [CrossRef]
72. Udo, S.O.; Aro, T.O. New empirical relationships for determining global PAR from measurements of global solar radiation, infrared radiation or sunshine duration. *Int. J. Climatol.* **2000**, *20*, 1265–1274. [CrossRef]
73. Alados, I.; Foyo-Moreno, I.y.; Alados-Arboledas, L. Photosynthetically active radiation: Measurements and modelling. *Agric. For. Meteorol.* **1996**, *78*, 121–131. [CrossRef]
74. Jacovides, C.P.; Timvios, F.S.; Papaioannou, G.; Asimakopoulos, D.N.; Theofilou, C.M. Ratio of PAR to broadband solar radiation measured in Cyprus. *Agric. For. Meteorol.* **2004**, *121*, 135–140. [CrossRef]
75. Alshaibani, K. Finding frequency distributions of CIE Standard General Skies from sky illuminance or irradiance. *Light. Res. Technol.* **2011**, *43*, 487–495. [CrossRef]
76. Li, D.H.W.; Cheung, G.H.W. Average daylight factor for the 15 CIE standard skies. *Light. Res. Technol.* **2006**, *38*, 137–152. [CrossRef]
77. Li, D.H.W.; Lam, T.N.T.; Cheung, K.L.; Tang, H.L. An analysis of luminous efficacies under the CIE standard skies. *Renew. Energy* **2008**, *33*, 2357–2365. [CrossRef]
78. Li, D.H.W.; Tang, H.L.; Wong, S.L.; Tsang, E.K.W.; Cheung, G.H.W.; Lam, T.N.T. Skies classification using artificial neural networks (ANN) techniques. In Proceedings of the 6th International Conference on Indoor Air Quality, Ventilation and Energy Conservation in Buildings: Sustainable Built Environment, IAQVEC 2007, Sendai, Japan, 28–31 October 2007; pp. 61–68.
79. Torres, J.L.; de Blas, M.; García, A.; Gracia, A.; de Francisco, A. Sky luminance distribution in the North of Iberian Peninsula during winter. *J. Atmos. Sol. Terr. Phys.* **2010**, *72*, 1147–1154. [CrossRef]
80. Tregenza, P.R. Analysing sky luminance scans to obtain frequency distributions of CIE Standard General Skies. *Light. Res. Technol.* **2004**, *36*, 271–279. [CrossRef]
81. Granados-López, D.; García-Rodríguez, A.; García-Rodríguez, S.; Suárez-García, A.; Díez-Mediavilla, M.; Alonso-Tristán, C. Pixel-based image processing for cie standard sky classification through ANN. *Complexity* **2021**, *310*, 108627. [CrossRef]
82. Suárez-García, A.; Granados-López, D.; González-Peña, D.; Díez-Mediavilla, M.; Alonso-Tristán, C. Seasonal caracterization of CIE standard sky types above Burgos, northwestern Spain. *Sol. Energy* **2018**, *169*, 24–33. [CrossRef]
83. García-Rodríguez, A.; Granados-López, D.; García-Rodríguez, S.; Díez-Mediavilla, M.; Alonso-Tristán, C. Modelling Photosynthetic Active Radiation (PAR) through meteorological indices under all sky conditions. *Agric. For. Meteorol.* **2021**, *310*, 108627. [CrossRef]